ACS OMEGA

Open Access

http://pubs.acs.org/journal/acsodf

Article

Design and Optimization of High-Performance Novel $RbPbBr_3$-Based Solar Cells with Wide-Band-Gap S-Chalcogenide Electron Transport Layers (ETLs)

Md. Selim Reza, Md. Ferdous Rahman,* Abdul Kuddus,* Mustafa K. A. Mohammed, Debashish Pal, Avijit Ghosh,* Md. Rasidul Islam, Sagar Bhattarai, Ibrahim A. Shaaban, and Mongi Amami

Cite This: *ACS Omega* 2024, 9, 19824−19836

Read Online

ACCESS | Metrics & More | Article Recommendations

ABSTRACT: Inorganic cubic rubidium−lead-halide perovskites have attracted considerable attention owing to their structural, electronic, and unique optical properties. In this study, novel rubidium−lead-bromide ($RbPbBr_3$)-based hybrid perovskite solar cells (HPSCs) with several high-band-gap chalcogenide electron transport layers (ETLs) of In_2S_3, WS_2, and SnS_2 were studied by density functional theory (DFT) and using the SCAPS-1D simulator. Initially, the band gap and optical performance were computed using DFT, and these results were utilized for the first time in the SCAPS-1D simulator. Furthermore, the impact of different major influencing parameters, that is, the thickness of the layer, bulk defect density, doping concentration, and defect density of interfaces, including the working temperature, were also investigated and unveiled. Further, a study on an optimized device with the most potential ETL (SnS_2) layer was performed systematically. Finally, a comparative study of different reported heterostructures was performed to explore the benchmark of the most recent efficient $RbPbBr_3$-based photovoltaics. The highest power conversion efficiency (PCE) was 29.75% for the SnS_2 ETL with V_{oc} of 0.9789 V, J_{sc} of 34.57863 mA cm^{-2}, and fill factor (FF) of 87.91%, while the PCEs of 21.15 and 24.57% were obtained for In_2S_3 and WS_2 ETLs, respectively. The electron−hole generation, recombination rates, and quantum efficiency (QE) characteristics were also investigated in detail. Thus, the SnS_2 ETL shows strong potential for use in $RbPbBr_3$-based hybrid perovskite high-performance photovoltaic devices.

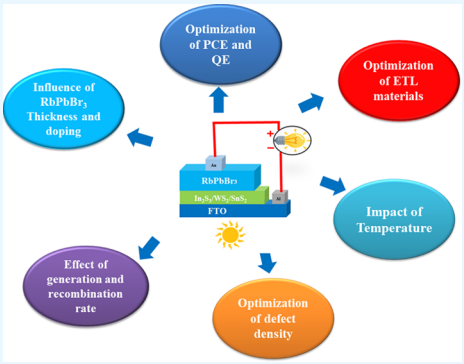

1. INTRODUCTION

A significant breakthrough in the field of photovoltaics has been made possible by the development of perovskite materials as possible replacements for efficient solar cell technology. Perovskite from the A_3MX_3 (where A is a larger size inorganic cation, M is a smaller metal cation, and X is an anion) group has lately emerged as a standout candidate, revealing remarkable characteristics that make it very well suited for solar energy conversion applications.[1−6] On the other hand, recently, ABX_3 (A and B are cations, and "X" is an anion)-type perovskite is also used for applications involving the conversion of solar energy. Perovskites are ideal for a variety of applications, including photovoltaics, optoelectronics, catalysis, and energy storage due to their exceptional properties, which include high electron and ion mobility, tunable band gap, and efficient light absorption.[7−10] The scientific community is very much interested in perovskite materials because they may be used to achieve an outstanding performance of PV (photovoltaic) solar cells.[11−15] Perovskite-based organic−inorganic hybrid solar cells (HPSCs), which have high light absorption, low defect density, long charge-carrier lifespan, high charge-carrier flexibility, and low stimulation binding energies, are significantly advancing device design and element control.[16−20] These organic cations' volatility and thermal instability represent the biggest interruption to their wide-ranging commercial applications.[21] However, inorganic $RbPbBr_3$ can significantly speed up advancing the fabrication of perovskite hybrid solar panels (cells) owing to their exceptional electronic and optical properties.[22] $RbPbBr_3$ has a suitable band gap (~1.31 eV) and a high absorption coefficient of ~10^5 cm^{-1} with enhanced thermal stabilities and structurally inflexible phases at room temperature.[23−26] A suitable choice of efficient electron transport layers (ETLs), an insertion of favorable element ions into the $RbPbBr_3$ host lattices, is an efficient approach to obtaining improved PV performance.[27−29] The ETL offers the

Received: October 21, 2023
Revised: January 16, 2024
Accepted: January 22, 2024
Published: April 22, 2024

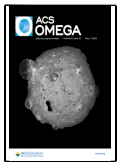

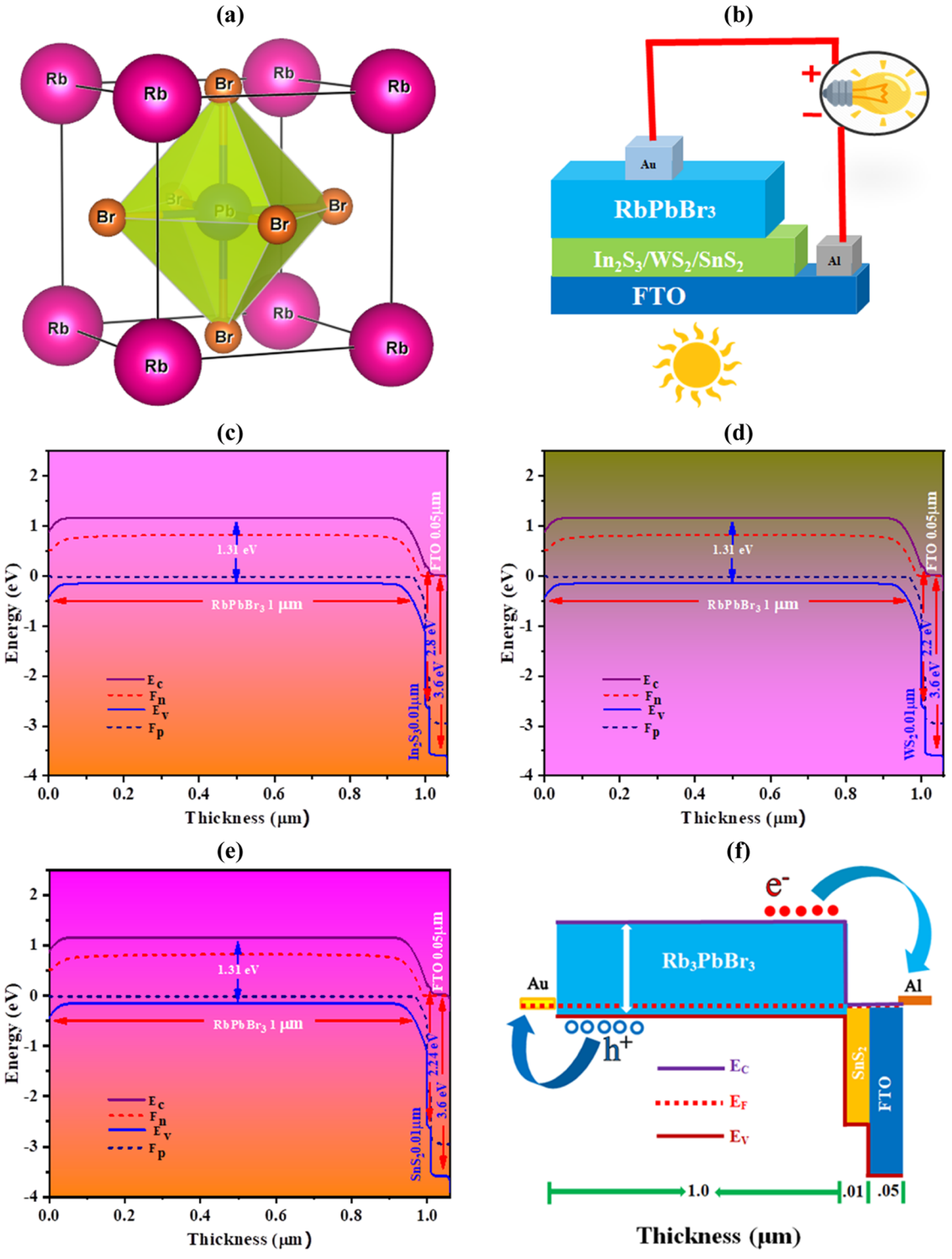

Figure 1. (a) Crystal structure of $RbPbBr_3$, (b) device structure, (c) energy band diagram with the In_2S_3 ETL, (d) energy band diagram with the WS_2 ETL, (e) energy band diagram with the SnS_2 ETL, and (f) the energy band alignment with the optimized structure (Al/FTO/SnS_2/$RbPbBr_3$/Au).

easiest pathway for transporting electrons through the perovskite surface to an electrode preventing the recombination of electrons and holes notably and ensuring loss-free passing of incident solar spectra.[30,31] Several solar cell architectures have been developed and put forth to date; however, when compared to different $RbPbBr_3$-heterostructure variants, their PCEs are found to be as high as expected.[32,33] The two-dimensional (2D) chalcogenide sulfur (S)-based ETLs of In_2S_3, WS_2, and SnS_2 have been found to be promising for $RbPbBr_3$ heterostructure photovoltaics. Among them, SnS_2, with a band gap of up to 1.6−2.24 eV and an absorption coefficient of $\sim 10^5$ cm^{-1}, appears to be one of the best potential materials as an ETL for fabricating high-efficiency solar cells, retaining the large ability for charge transmission as well as accumulation with a well-aligned band structure. The wide-band-gap SnS_2 has also shown high electron flexibility

https://doi.org/10.1021/acsomega.3c08285
ACS Omega 2024, 9, 19824−19836

and rigidity with the visible wavelengths of the light spectrum, thereby efficiently transporting carriers from the photoactive layers to the electrode, resulting in boosting the overall device performance.[34]

In this study, $RbPbBr_3$-based hybrid perovskite solar cells (HPSCs) with several chalcogenide ETLs of In_2S_3, WS_2, and SnS_2 have been studied. Initially, the impact of different major influencing parameters, namely, the layer thickness, bulk defect density, doping concentration, and interface defect density, including the working temperature, were investigated and unveiled. After that, a systematic study of an optimized device with the most potential ETL (SnS_2) layer was performed. Finally, a comparative study on different reported heterostructures was performed to design the most recently developed efficient $RbPbBr_3$-based photovoltaics. However, the SnS_2 ETL is not only suitable for Rb-based PSC devices but can also be used in many other types of PSCs with outstanding performance, such as $CsPbI_3$, $FAPbI_3$, $MAPbI_3$, $FAMAPbI_3$, Sr_3SbI_3, Sr_3PI_3, and Ca_3NI_3.[35−39]

2. CONSTRUCTION AND SIMULATION METHODOLOGY

A one-dimensional solar cell capacitance simulator (SCAPS) application was used for the simulation to examine the proposed Al/FTO/ETLs (In_2S_3, WS_2, or SnS_2)/$RbPbBr_3$/Au photovoltaic cells, assigned as Devices I (SnS_2), II (WS_2), and III (In_2S_3), respectively. At the Electronic and Information Systems Department of the University of Ghent, Belgium, SCAPS-1D software was invented. By resolving fundamental equations, continuity equations for electrons and holes, and electrostatic potential equations under steady-state conditions, both structures were anticipated and analyzed systematically.[40,41] Figure1a shows the crystal structure of an inorganic cubic $RbPbBr_3$ perovskite. Figure 1b shows the symmetric structures of devices I−III at a given time. The PV cell consisted of a p-type absorber layer, a highly doped n-type ETL (In_2S_3, WS_2, or SnS_2) layer with an FTO window layer and an Au back-metal electrode. Figure1c−e shows the energy band diagram (EBD) with an illustration of the carrier dynamics for the corresponding devices, and Figure1f shows the energy band alignment with the optimized structure of (Al/FTO/SnS_2/$RbPbBr_3$/Au). The electron−hole pair formation within the device is confirmed by the specific positions of quasi-Fermi states Fn and Fp under illumination. The generation of electron−hole pairs within the device is confirmed by the offset between the absorber VB and CB. The difference in the work function (WF) between the absorber and transmission layers is the cause of the observed offset. At the absorber/ETL interface, the integrated voltage and related fields of electricity assist in the separation of the generated light.

3. RESULTS AND DISCUSSION

3.1. Band Structure. The band structure of the $RbPbBr_3$ perovskite with the Brillouin zone path Γ−*X*−*M*−*R*−Γ is shown in Figure 2. Using the GGA-PBE function, we obtained a band gap of 1.31 eV at the *R*-point in Figure 2. The GGA-PBE function produces more reasonable results. We indicated the energy levels from −5 to +5 eV, and at point *R*, the material's band structure reveals a direct gap with a value of 1.31 eV, with the vertical line representing the Fermi level (E_f) = 0 eV. The material's direct band gap is caused by an unusual

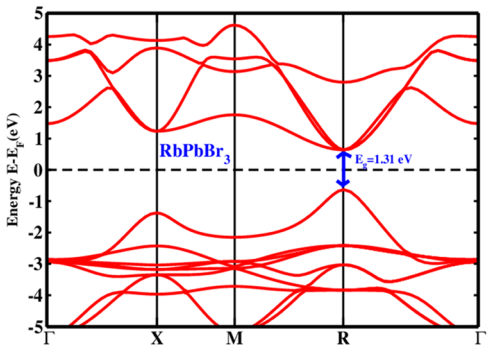

Figure 2. Band structure of the $RbPbBr_3$ perovskite.

occurrence where the highest energy level of the valence band coincides precisely with the lowest energy level of the conduction band at a specific symmetry point (*R*). The material's high absorption coefficient is due to this straight band gap.

3.2. Optical Properties. Figure 3a,b illustrates the optical characteristics of the $RbPbBr_3$ perovskite, including the optical absorption and the imaginary and real components of the dielectric function. The optical absorption coefficient is an essential indicator of how well a material is able to absorb light energy and offers compelling evidence in favor of solar efficiency.[39,42−44] The profile of the optical absorption coefficient displays traits that are reminiscent of the imaginary component of the dielectric constant for all configurations. The greatest peak in the optical absorption spectrum can be found for the $RbPbBr_3$ perovskite structures in the visible region. Figure 3a demonstrates the absorption coefficient of the $RbPbBr_3$ perovskite structures as a function of the photon energy. The optical properties of $RbPbBr_3$ that have been studied here show a good fit with the previously reported results.[30,45]

The complex dielectric function, which is energy- or frequency-dependent, is transformed using the Kramers−Kronig eq 1

$$\varepsilon(\omega) = \varepsilon_1(\omega) + i\varepsilon_2(\omega) \quad (1)$$

where the real part is defined by $\varepsilon_1(\omega)$ and the imaginary part is defined by $i\varepsilon_2(\omega)$.

The real portion of the dielectric constant can be used to calculate the dispersion effects and polarization. The zero-frequency limit, $\varepsilon_1(0)$, which corresponds to the electronic component of the real dielectric function, is the best essential quantity in the real part $\varepsilon_1(\omega)$. For cubic $RbPbBr_3$, the computed $\varepsilon_1(0)$ value is 5.8. The values of the real part $\varepsilon_1(\omega)$ began to increase from $\varepsilon_1(0)$, first reaching the highest value, after which they decreased and produced many peaks. In general, large band gap materials have a lower peak dielectric constant value than low band gap materials. The imaginary component of the dielectric function is a crucial property for assessing the optical absorption and the ability of crystal structures to store energy from neutral charge excitations. Furthermore, the imaginary portion $\varepsilon_2(\omega)$ is closely tied to the system's band structure. The $\varepsilon_2(\omega)$ values of $RbPbBr_3$ suggest a broad absorption spectrum. The transition of carriers from the VB to the CB is shown by the peaks of the imaginary component of the dielectric constant.

Table 1 demonstrates simulation parameters for the active materials of FTO, In_2S_3, WS_2, SnS_2, and $RbPbBr_3$, which were

https://doi.org/10.1021/acsomega.3c08285
ACS Omega 2024, 9, 19824−19836

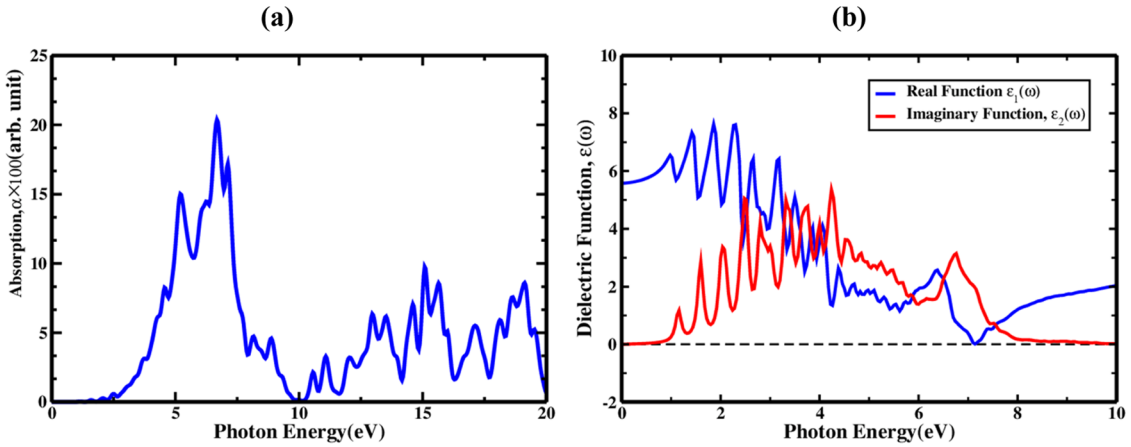

Figure 3. (a) Optical absorption and (b) the imaginary and real parts of the dielectric function.

Table 1. Input Parameters of the FTO, ETL, and Absorber Layer

parameters	FTO[48]	In_2S_3[47,49]	WS_2[30,46]	SnS_2[34]	$RbPbBr_3$[23]
thickness (nm)	50	10	10	10	1000
band gap, E_g (eV)	3.6	2.8	2.20	2.24	1.31
electron affinity, χ (eV)	4.5	4.45	4.5	4.24	4
dielectric permittivity (relative), ϵ_r	10	13.5	13.6	10	5.8
CB effective density of states, N_C (1/cm^3)	2×10^{18}	1.8×10^{19}	2.8×10^{18}	2.2×10^{18}	7.6×10^{18}
VB effective density of states, N_V (1/cm^3)	1.8×10^{19}	4×10^{13}	1.9×10^{19}	1.8×10^{19}	2×10^{19}
electron thermal velocity (cm s^{-1})	1×10^7	1×10^7	1×10^7	1×10^7	1×10^7
hole thermal velocity (cm s^{-1})	1×10^7	1×10^7	1×10^7	1×10^7	1×10^7
electron mobility, μ_n (cm^2 V^{-1} s^{-1})	100	400	100	50	50
hole mobility, μ_h (cm^2 V^{-1} s^{-1})	20	210	100	50	50
shallow identical acceptor density, N_A (1/cm^3)	0	0	0	0	1×10^{17}
shallow identical donor density, N_D (1/cm^3)	1×10^{18}	1×10^{17}	1×10^{17}	1×10^{17}	0
defect density, N_t (1/cm^3)	1×10^{12}	1×10^{12}	1×10^{12}	1×10^{12}	1×10^{12}

collected from the previous notable literature, and the realistic thermal velocity of the electrons and holes were fixed at 10^7 cm s^{-1}.[23,30,34,46,47] The back and front electrodes were made of gold (Au) and aluminum (Al) having WFs of 5.37 eV (110) and 4.2 eV (100), respectively. Table 2 lists the parameters of the absorber/ETL interface used for each of the three proposed photovoltaic devices.

Table 2. Data for Interface Parameters Used in the $RbPbBr_3$-Based Solar Cells

parameters	$RbPbBr_3$/In_2S_3	$RbPbBr_3$/WS_2	$RbPbBr_3$/SnS_2
defect type	neutral	neutral	neutral
σ_e (cm^2)	1×10^{19}	1×10^{19}	1×10^{19}
σ_h (cm^2)	1×10^{19}	1×10^{19}	1×10^{19}
E_r	0.6	0.6	0.6
total defect density (cm^{-1})	10^{10}–10^{20}	10^{10}–10^{20}	10^{10}–10^{20}
energetic distribution	single	single	single
working temperature (K)	275–400	275–400	275–400

3.3. Optimization of Thickness and Charge-Carrier Concentration of the Absorber Layer. Figure 4a shows the impact of variation of the absorber layer thickness of 100–2000 nm to obtain the optimized performance of the proposed devices while keeping the other parameters unchanged, as demonstrated in Table 2. The carrier generation as well as substantial recombination rates increase with increasing thickness of the absorber layer noticeably. With increasing absorber layer thickness, the open-circuit voltage and V_{oc} of the PSC increased for every configuration of the three different ETLs. A value of 0.95 V was obtained within device I for the SnS_2 configuration, though the increment rate was high (from 0.69 to 0.84 V) for device III (In_2S_3). Similarly, the short-circuit current (J_{sc}) increased with increasing thickness of the absorber layer, owing to improved spectral absorption, especially at longer wavelengths. The J_{sc} increased from 12 to 32.77 mA cm^{-2} for device III, from 17.025 to 35.14 mA cm^{-2} for device I, and from 19.34 to 35.12 mA cm^{-2} for device II. The saturated spectral absorption and domination of charge-carrier recombination at a thick absorber layer of ≥1000 nm for each of the three configurations. These changes in V_{oc} and J_{sc} are consistent with those reported in previous articles.[50−52] The cell fill factor (FF) is almost unchanged at 87 and 79% for devices I and II, respectively, while it increases from 68 to 85% for device III with increasing absorber layer thickness. A PSC usually operates at its maximum value when the absorber layer thickness and charge-carrier diffusion length are equal.

A higher number of photons are absorbed in a thick absorber layer; however, the rate of recombination also increases simultaneously. Thus, a proper equilibrium is essential within the absorption of light and separation of bearers to obtain high performance.[53−55] With a series of simulations, the V_{oc} values of 0.951, 0.897, and 0.8267 V, J_{sc} values of 34.55, 34.5548, and 30.22 mA cm^{-2}, FF values of 87.49, 79.05, and 84.46%, and consequently, the PCE values of

https://doi.org/10.1021/acsomega.3c08285
ACS Omega 2024, 9, 19824−19836

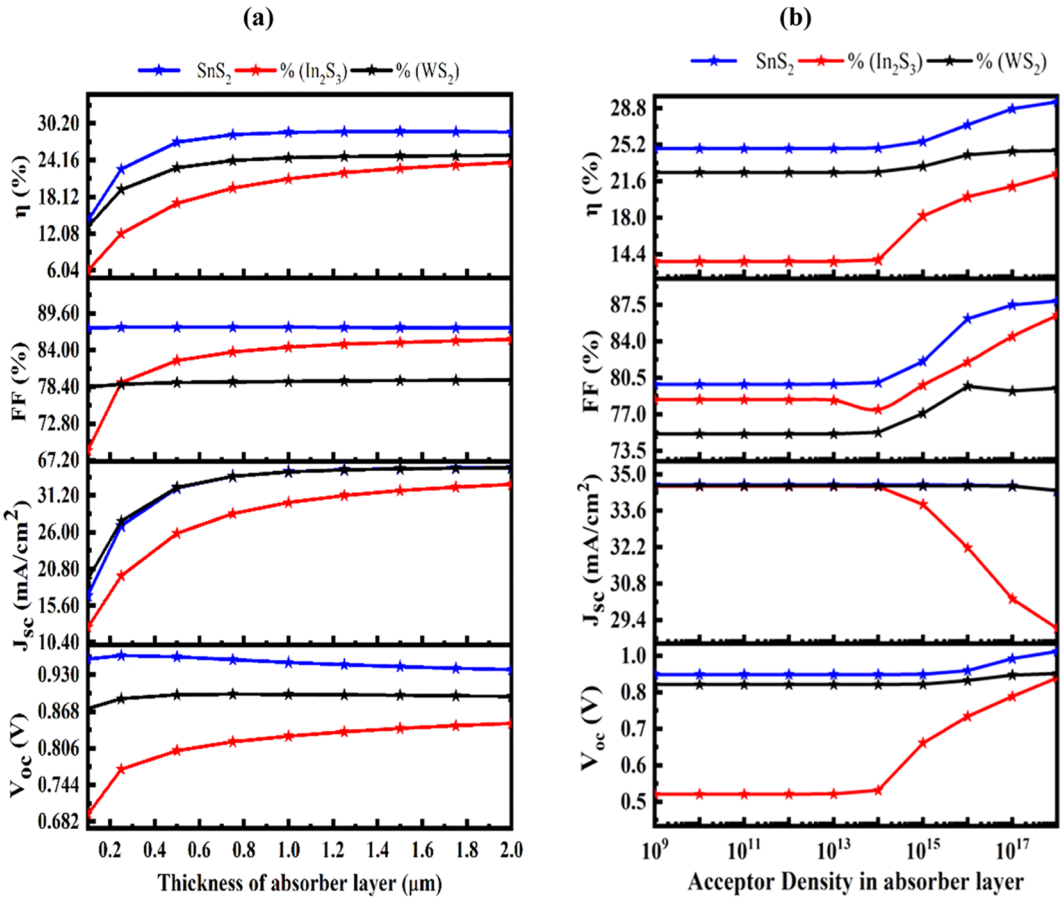

Figure 4. Impact of variation in (a) absorber layer thickness and (b) doping density of the absorber on the PV parameters V_{oc}, J_{sc}, FF, and PCE.

28.75, 24.56, and 21.11%, were obtained at an optimal $RbPbBr_3$ absorber layer thickness of ∼1000 nm for the SnS_2, WS_2 and In_2S_3 ETL configurations, respectively.

Figure 4b illustrates the changes in the electronic parameters of V_{oc}, J_{sc}, FF, and PCE with the acceptor-doping density (N_A) of the $RbPbBr_3$ absorber from 10^9 to 10^{18} cm^{-3} for the three proposed configurations. During optimization, the V_{oc} of the PSC remained almost unchanged up to an N_A of 10^{14} cm^{-3}. At higher N_A, i.e., beyond N_A of 10^{14} cm^{-3}, the V_{oc} tends to increase, which leads to a lower shift in the Fermi energy level of the hole, resulting in improved built-in potential.[56] The V_{oc} reaches up to 0.97 and 0.90 V for devices I and II, while it is 0.88 V for device III with a relatively higher rate of change. Similar behavior was also observed for FF with noticeable (2−3%) improvement, reaching almost saturated values of 87.49, 79.23, and 84.46% for the SnS_2, WS_2, and In_2S_3 ETL configurations, respectively, at a N_A of 10^{17} cm^{-3}, as summarized in Table 3 These results were consistent with those of previous reports.[57,58]

Table 3. PV Characteristics of Solar Cells Based on $RbPbBr_3$ are Compared with Different ETLs

parameters	SnS_2	WS_2	In_2S_3
thickness (nm)	10	10	10
V_{OC} (V)	0.951	0.8967	0.8267
J_{SC} (mA cm^{-2})	34.5542	34.5466	30.22143
FF (%)	87.49	79.23	84.46
PCE (%)	28.75	24.56	21.1

3.4. Optimization Thickness of Various ETLs. Figure 5 shows the effects of SnS_2, WS_2, and In_2S_3 ETL thicknesses on the PV parameters in the range of 10−500 nm, keeping the remaining adjusted parameters unchanged, as demonstrated in the aforementioned tables. An insignificant change in the PV parameters was observed when varying the ETL thicknesses in the range of 10−500 nm.

Consequently, V_{oc}, J_{sc}, FF, and PCE changed from 0.95 to 0.9498 V, 34.55 to 34.6993 mA cm^{-2}, 87.49 to 87.53%, and 28.75 to 28.85%, respectively, for the SnS_2 ETL. For the WS_2 ETL, J_{sc} slightly improved from 34.55 to 34.554 mA cm^{-2}, while the FF and PCE decreased from 79.23 to 79.05% and 24.56 to 24.49%, respectively. Similarly, J_{sc}, FF, and PCE changed from 30.22143 to 30.34129 mA cm^{-2}, 84.46 to 84.32%, and 21.1 to 21.15%, respectively, for the In_2S_3 ETL. However, for both the WS_2 and In_2S_3 ETLs, the value of V_{oc} remained constant. Such independence of the ETL thickness over a wide range exposes the versatility of the practical film fabrication for application to the proposed device structures. Moreover, considering the sufficient spectral transparency of the ETL and practical thin-film fabrication challenges, we chose an optimum thickness of 10 nm for further study.

3.5. Optimization Donor Density and Bulk Defect Density of the SnS_2 ETL. Figure 6a depicts the effect of variation in the doping concentration (N_D) of the SnS_2 ETL on the PV parameters in the range of 1×10^{10} to 1×10^{20} cm^{-3}. The V_{oc} remained almost the same up to $N_D = 1 \times 10^{17}$ cm^{-3}, and it started to decrease (from 0.979 to 0.9786) when N_D increased over 1×10^{17} cm^{-3}, while the J_{sc} and FF

https://doi.org/10.1021/acsomega.3c08285
ACS Omega 2024, 9, 19824−19836

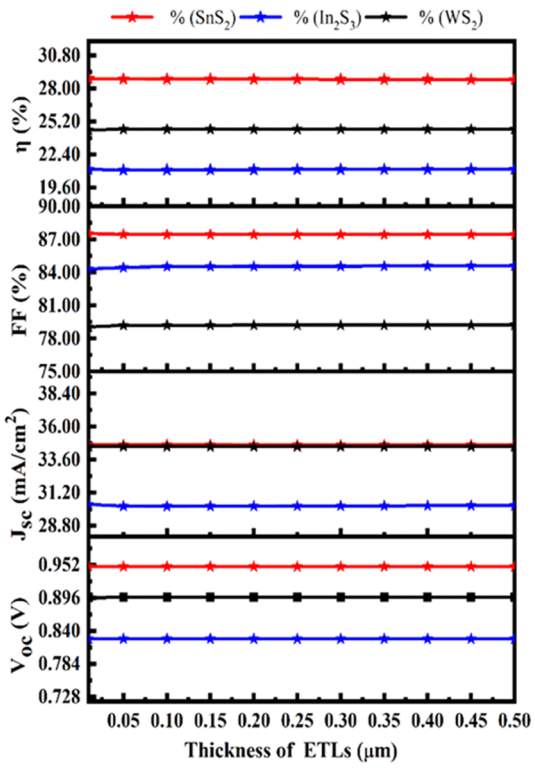

Figure 5. Thickness effects of various ETLs.

remained constant at 34.58 mA cm^{-2} and 87.91%, respectively. A similar trend was observed for the three structures corresponding to changes in N_D.[5050] Thus, the optimum value of N_D of the ETL was chosen to be 10^{17} cm^{-3} considering the realistic behavior of SnS_2 thin films for the next stages of this study.

Figure 6b shows how the N_t (bulk defect density) of the SnS_2 ETL impacts the effectiveness of the proposed structure. The V_{oc}, J_{sc}, FF, and consequently, the PCE remained nearly constant up to $N_t = 10^{18}$ cm^{-3}, while the N_t of SnS_2 increased from 10^{12} to 10^{20} cm^{-3}, showing notable vulnerability gain defects. Thereafter, the FF started to decrease from 87.91 to 87.24%, resulting in a reduction in the PCE from 29.74 to 29.48% for increasing N_t from 10^{18} to 10^{20} cm^{-3}. This behavior of PV parameters was found to be consistent with a previous report.[51] Thus, the N_t of 10^{17} cm^{-3} was chosen as an ideal value for further study in later sections.

3.6. Influence of Layer Thickness and Defect Density Variation of the $RbPbBr_3$ Absorber on PV Performance.

Figure 7 shows the change in the defect density and thickness of the $RbPbBr_3$ absorber layer from 10^{10} to 10^{18} cm^{-3} and from 0.1 to 2.0 μm, respectively, to examine the effect of defect density on solar cell performance. The solar cell performance metrics degrade dramatically when the $RbPbBr_3$ defect density exceeds 10^{12} cm^{-3}.[51] The ETA, FF, J_{sc}, and V_{oc} of the Al/FTO/SnS_2/$RbPbBr_3$/Au structures decrease from 30.33 to 9.44%, 87.91 to 61.66%, 35.2 to 20.17 mA cm^{-2}, and 0.98 to 0.7592 V, respectively, when the bulk defect density and absorber layer thickness are altered from 10^{10} to 10^{18} cm^{-3} and 0.1 to 2.0 μm. According to Figure 7a, the highest V_{oc} of 0.98 V is achieved when the thickness is above 1 μm, and the defect density is below 1×10^{12} cm^{-3}. However, when the defect density exceeds 10^{12} cm^{-3}, V_{oc} significantly drops to 0.7592 V. According to Figure 7b, the thickness must be greater than 1 μm, and the defect density must be lower than 10^{12} cm^{-3} in

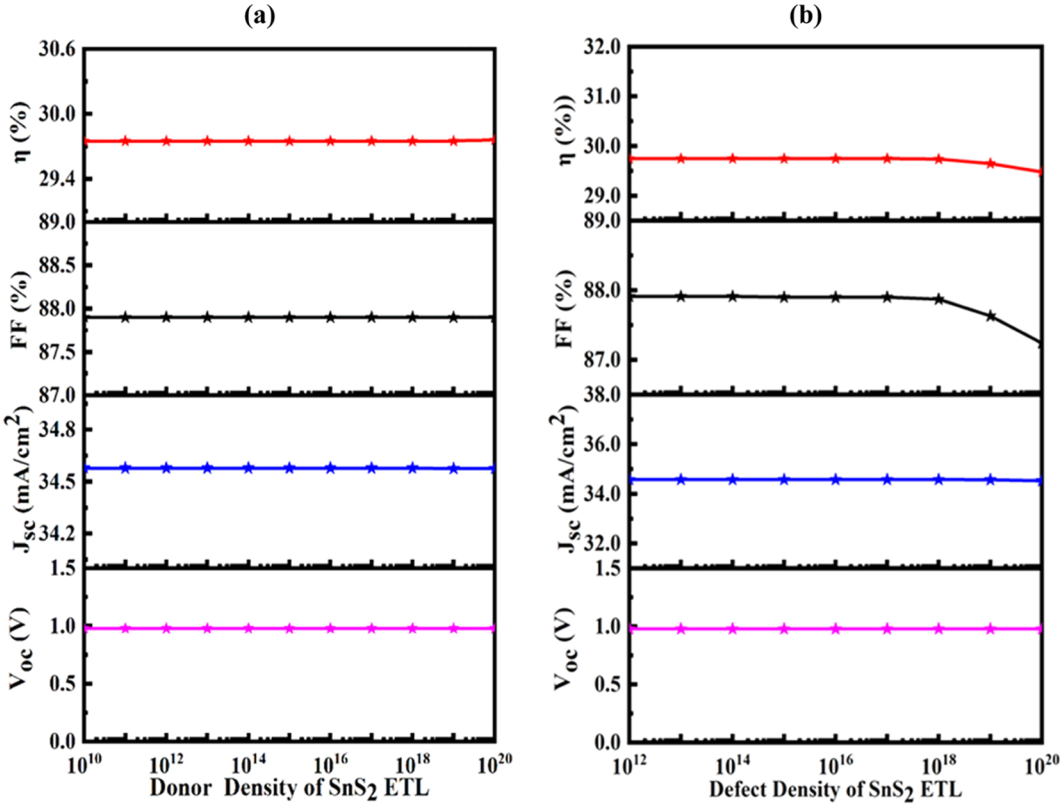

Figure 6. Impact of variation of (a) donor density and (b) bulk defect density of the SnS_2 ETL.

https://doi.org/10.1021/acsomega.3c08285
ACS Omega 2024, 9, 19824−19836

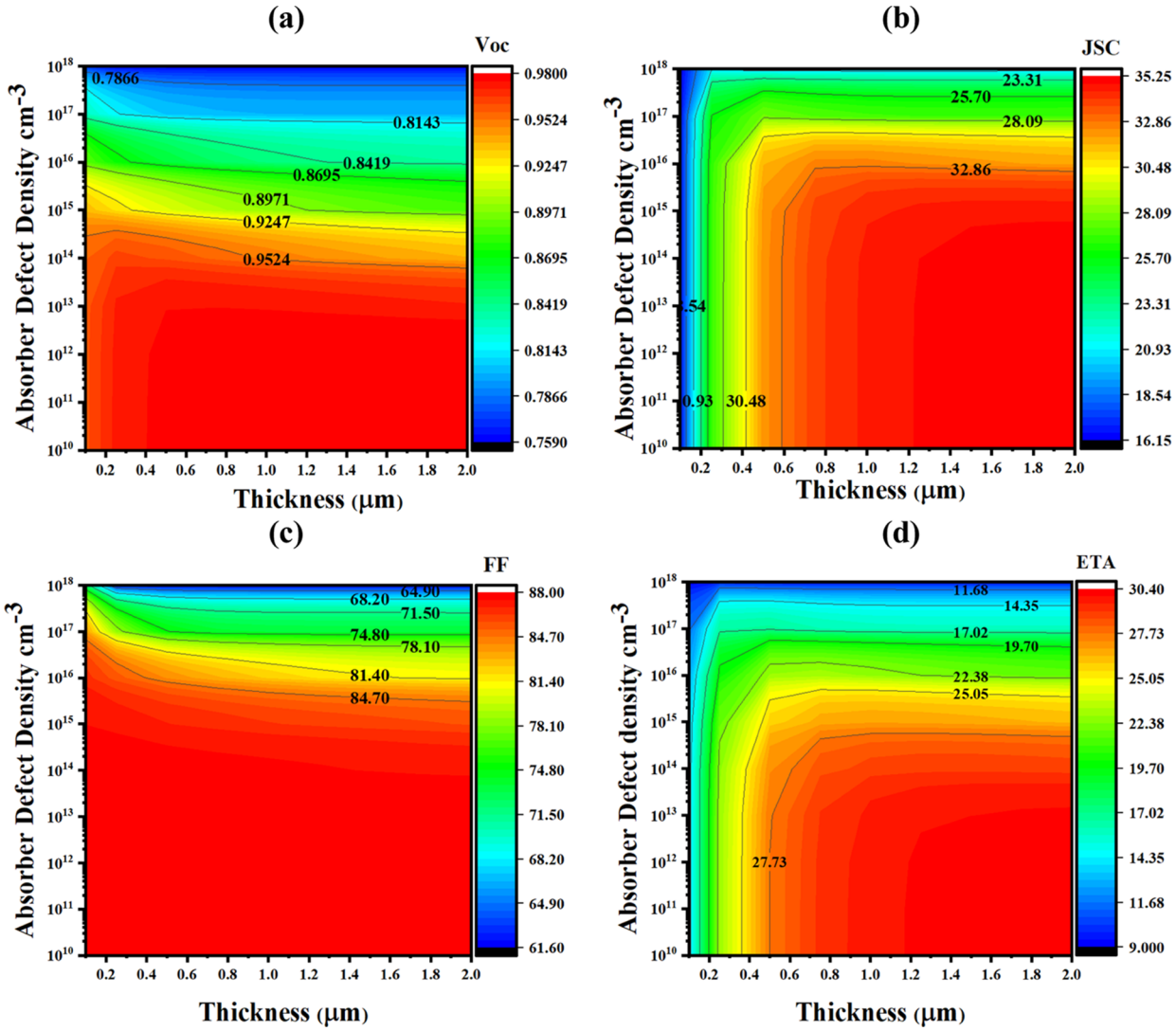

Figure 7. Effects of absorber thickness and defect density variations on photovoltaic performance parameters: (a) V_{oc}, (b) J_{sc}, (c) FF, and (d) ETA.

order to reach the highest J_{sc} value of 35.2 mA cm^{-2}. Figure 7c shows that the FF reaches its maximum value of 87.91% when the thickness is greater than or equal to 1 μm, and the defect density is less than or equal to 10^{12} cm^{-3}. However, if the defect density increases beyond 10^{12} cm^{-3}, the FF sharply drops to 61.66%.

Figure 7d demonstrates that the thickness range of 0.25−2.0 μm and the defect density of up to 10^{12} cm^{-3} have resulted in the greatest conversion efficiency, exceeding 29%. The introduction of high defect states in the absorber layer results in a high carrier recombination rate in the cell, which in turn leads to a reduction in cell performance.[59−61] The best combination of parameters for achieving the highest possible PCE of 29.75% has been identified, which includes a constant thickness of 1.0 μm for the $RbPbBr_3$ absorber layer and a defect concentration of 10^{12} cm^{-3}. At these values, the solar cell achieved a V_{oc} of 0.9789 V, a J_{sc} of 35.57863 mA/cm^2, and an FF of 87.91%.

3.7. Influence of Layer Thickness and Interface Defect Density Variation of the $RbPbBr_3$ Absorber on PV Performance. The characteristics that control how light and electricity interact with one another can be changed by defects in the material system. The effectiveness of the cell is also significantly impacted by the quality of the interface. To investigate the impact of interface defect density on the performance of the $RbPbBr_3$-based solar cell, Figure 8 shows the changes in the defect density of the $SnS_2/RbPbBr_3$ interfaces from 10^{10} to 10^{18} cm^{-2} and in the thickness of the $RbPbBr_3$ absorber layer from 0.1 to 2.0 μm, respectively. When the interface defect density of $SnS_2/RbPbBr_3$ exceeds 10^{10} cm^{-2}, respectively, there is a notable decrease in the solar cell performance parameters. When the defect densities of the $SnS_2/RbPbBr_3$ interfaces are increased from 10^{10} to 10^{18} cm^{-2} and the absorber layer thickness is increased from 0.1 to 2.0 μm, the values of ETA, FF, J_{sc}, and V_{oc} decrease.

The following values decrease, in particular: ETA (30.29−4.92%), FF (87.9−61.48%), J_{sc} (35.08993 to 35.20497 mA cm^{-2}), and V_{oc} (0.979 to 0.2282 V). The V_{oc} values are shown in Figure 8a. Figure 8b demonstrates that the maximum value of J_{sc}, which is 35.20497 mA cm^{-2}, is attained at a thickness of 2.0 μm and a defect density below 1×10^{14} cm^{-2}. When the thickness of the absorber is 1.0 μm, the interface defect density is less than or equal to 10^{14} cm^{-2}. Figure 8c illustrates that the FF achieves its highest value of 87.9%. However, FF considerably decreases to 61.48% when the interface defect density reaches 10^{14} cm^{-2}, and the absorber thickness is less

https://doi.org/10.1021/acsomega.3c08285
ACS Omega 2024, 9, 19824−19836

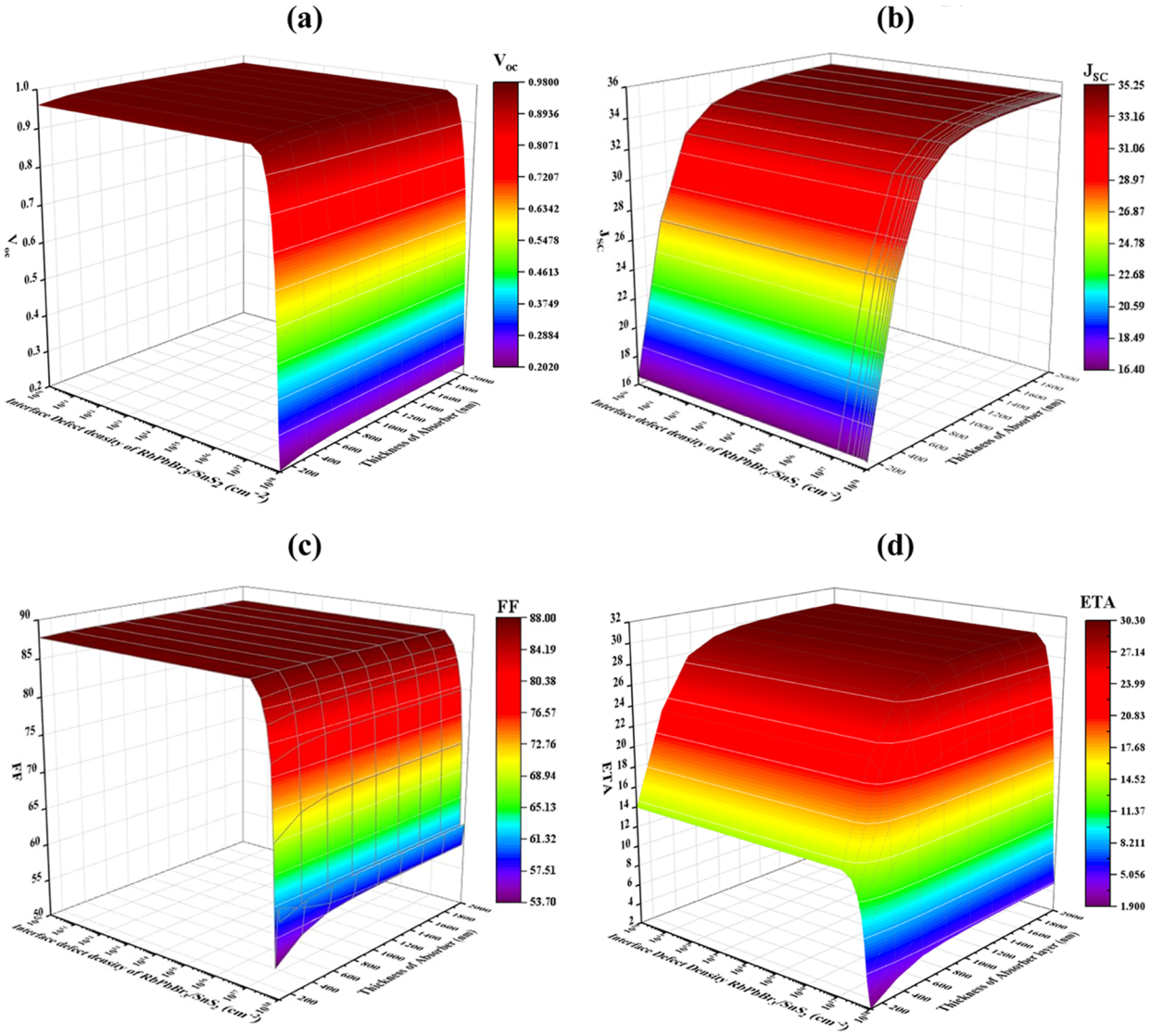

Figure 8. Effects of absorber layer thickness and interface defect density ($RbPbBr_3/SnS_2$) variations on photovoltaic performance parameters: (a) V_{oc} (b) J_{sc} (c) FF, and (d) ETA.

than or equal to 1.0 μm. According to Figure 8d, a maximum conversion efficiency of over 29.75% is attained when the thickness is between 0.1 and 2.0 μm, and the defect density is below 10^{16} cm^{-2}.

3.8. Analysis of Carrier Generation and Recombination. Figure 9a,b displays the carrier generation and recombination rates for the position in the optimized SnS_2/$RbPbBr_3$ heterostructure device, respectively. In the carrier generation process, electrons excited by incident photons in the VB jump to the CB, leaving a hole in the VB and producing electron−hole pairs. This carrier generation increases by the release of holes and electrons produced by these PSCs, which retain avalanche behaviors. For the modified structure, the highest generation rate was seen at a location of around 1 μm. The higher photon absorption at that particular position resulted in the highest rate of generation in that region (absorber layer). Herein, an almost linear total generation was obtained in the optimized $SnS_2/RbPbBr_3$ heterostructure with the highest value of over 10^{22} cm^3s^{-1}, while the highest total recombination value was observed at almost 10^{16} cm^2 s^{-1} simultaneously in similar regions. SCAPS-1D determines the generation of the pairs of electron−hole, $G(x)$, corresponding to the net flashing photon flux, $N_{phot}(\lambda, x)$, using eq 2 as follows

$$G(\lambda, x) = \alpha(\lambda, x) \cdot N_{phot}(\lambda, x) \quad (2)$$

However, holes and electrons of the CB fall in the recombination process after generation, having a shorter lifetime than their lifetime, owing to the presence of recombination centers (defects), higher carrier density, and longer diffusion length. This is because, in comparison to other regions, the greater number of electrons inside the CB cross the energy barrier and are shipped toward the VB, where they stabilize and occupy the exact location of a hole that exists. The energy levels generated by such events cause a noticeable effect on the recombination of the electron−hole profile. Additionally, the distribution rates of recombination may not be uniform due to grain boundaries and defects. Thus, defects and their distribution, carrier density, and duration of charge carriers have an impact on the rate of recombination in PSCs, which requires careful consideration during practical device fabrication with minimal recombination centers.

https://doi.org/10.1021/acsomega.3c08285
ACS Omega 2024, 9, 19824−19836

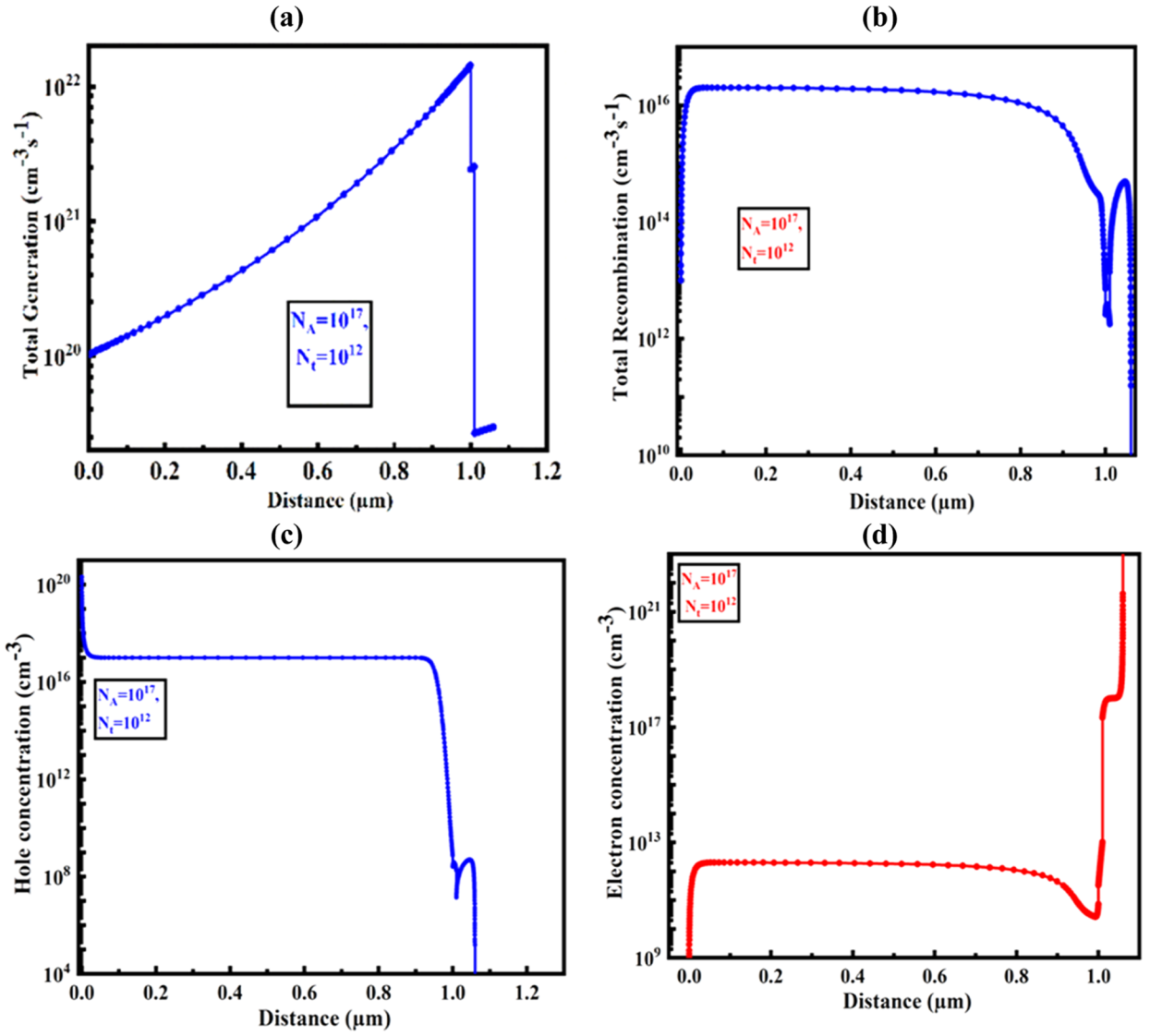

Figure 9. (a) Total generation, (b) total recombination, (c) hole concentration, and (d) electron concentration rate with respect to distance of the optimized device.

Figure 9c,d shows the hole and concentration rates for the positions in the optimized SnS_2/$RbPbBr_3$ heterostructure device. The effective density of states (DOS) in the valence bands and the hole concentration are caused by acceptor concentrations in the absorbers that are liable for net carrier mobility, which is undoubtedly beneficial for high-efficiency device fabrication.[62,63] A stable hole concentration of 10^{17} cm^{-3} throughout the absorber regions with a low electron concentration of 10^{12} cm^{-3} was obtained at optimized conditions under the chosen parameters demonstrated in previous tables. The hole mobility of $RbPbBr_3$ perovskite with less e-h recombination and a significant carrier generation rate was found to be an effective and promising absorber material for the fabrication of high-performance thin-film solar cells combined with a SnS_2 ETL.

3.9. Effect of Temperature on the Proposed Optimized $RbPbBr_3$-Based Perovskite. Figure 10 demonstrates the impact of the working temperature (WT) of the $RbPbBr_3$ perovskite on various PV parameters changing from 275 to 400 K. In the proposed SnS_2 ETL-based optimized device, V_{oc}, FF, and consequently, the PCE decreased from 1.014 to 0.8337 V, 88.98 to 83.21%, and 31.2 to 23.99%, respectively, while J_{sc} increased from 34.574 to 34.586 mA cm^{-2} corresponding to the change of WT from 275 to 400 K. An increase in the working temperature causes an acceleration of carrier velocity in random directions, which results in unwanted collisions as well as deformation stress; therefore, the carrier recombination domination occurs, resulting in a marked reduction of the cell performance.[64]

In contrast, as the temperature increases, the series resistance (R_s) increases, and the diffusion length reduces severely; therefore, the cell performance decreases markedly.[62,65] Though high performance occurs at 275 K, we consider 300 K to be an optimized value. Besides, this value is approximately close to the room temperature (298 K). Thus, the working temperature of ≤300 K was found to be a favorable range for obtaining high performance from the proposed device with the SnS_2 ETL.

3.10. Analysis of *J*–*V* and QE Properties of $RbPbBr_3$-Based Optimized Structures. Figure 11a exhibits the *J*–*V* (current density–voltage) graphs of the circuit at the absorber layer thickness in the range of 250–2000 nm with an

https://doi.org/10.1021/acsomega.3c08285
ACS Omega 2024, 9, 19824−19836

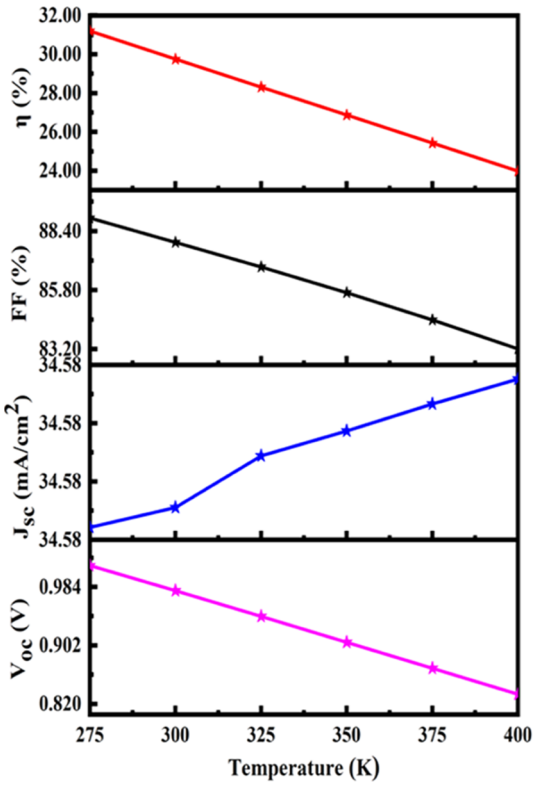

Figure 10. Effect of the working temperature of the $RbPbBr_3$-based optimized structure.

optimized N_A of 10^{17} cm^{-3}, N_t of 10^{12} cm^{-2}, and N_{int} of 10^{16} cm^{-2} of the proposed PSC. The optimum absorber thickness was found to be 1000 nm with a systematical analysis. The PCE was found to be 29.75% with V_{oc} of 0.979 V, J_{sc} of 34.58 mA cm^{-2}, and FF of 87.91% for SnS_2, while the PCE was 21.15 and 24.57% for In_2S_3 and WS_2 ETLs, respectively.

QE refers to a ratio of the photogenerated charge carriers to photons impacting the cell,[66−68] as shown in Figure 11b, for an absorber thickness range of 250−3000 nm. The QE reached almost saturation over the 1000 nm thickness of the absorber layer in the quantum efficiency (QE) curve of the corresponding devices. It sharply decreased from the highest value (∼99%) to zero, i.e., at the cutoff position of ∼950 nm (∼1.3 eV). Considering the trade-off among PV parameter values, the optimized thickness was chosen as 1000 nm. These QE spectra support the obtained $J-V$ characteristics.[69]

4. CONCLUSIONS

We designed and optimized inorganic $RbPbBr_3$-based perovskite solar cells for three different S-chalcogenide ETLs of SnS_2, WS_2, and In_2S_3 with a heterostructure of Al/FTO/ETL/$RbPbBr_3$/Au for the first time. The band gap alignment of $RbPbBr_3$ was found to match well with SnS_2 as an efficient electron transport compared to WS_2 and In_2S_3 ETLs after a systematic simulation. To obtain an optimized device performance and understand the charge transport characteristics, including electron−hole generation and recombination, several major influencing parameters, such as the thickness of the layer, bulk defect density, doping concentration, interfaces defect density, and working temperature, were investigated. Further, a study on the optimized device with the most potential ETL (SnS_2) layer was performed to explore the carrier generation and recombination behavior. Finally, a comparative study among PV parameters of the proposed optimized device and those reported in the literature was performed to explore the benchmark of efficient $RbPbBr_3$-based photovoltaics. The highest PCE was 29.75% for the SnS_2 ETL with V_{oc} of 0.979 V, J_{sc} of 34.58 mA cm^{-2}, and FF of 87.91%, while PCEs of 21.15 and 24.57% were obtained for the In_2S_3 and WS_2 ETLs, respectively. Additionally, the QE results validate the obtained outcomes. Thus, the SnS_2 ETL shows strong potential for use in future high-efficiency Rb-based PSC devices.

AUTHOR INFORMATION

Corresponding Authors

Md. Ferdous Rahman − *Advanced Energy Materials and Solar Cell Research Laboratory, Department of Electrical and Electronic Engineering, Begum Rokeya University, Rangpur*

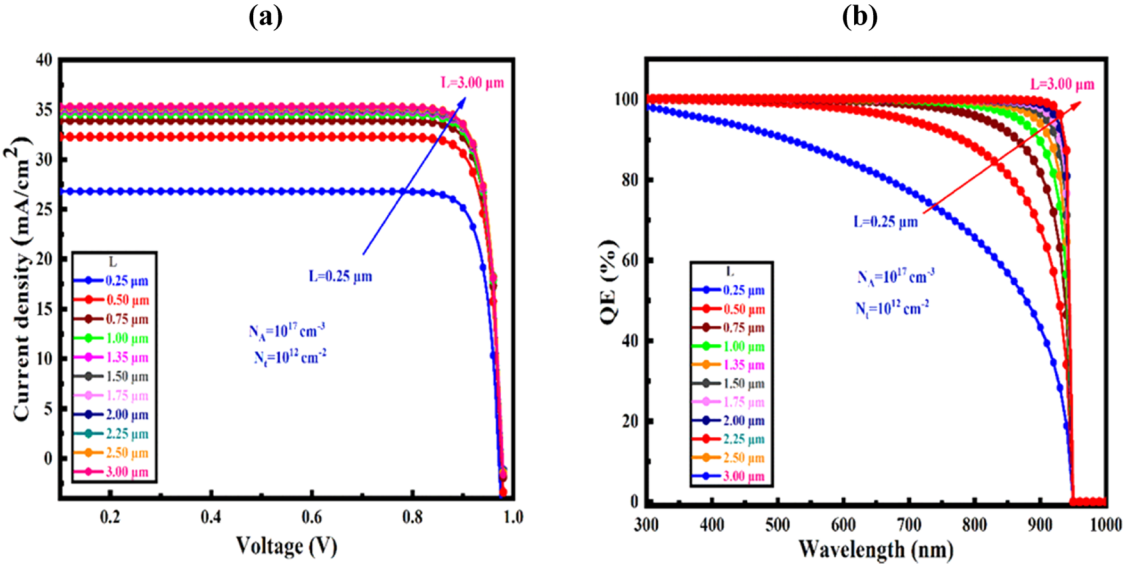

Figure 11. (a) $J-V$ and (b) QE curves of the proposed optimized structure.

https://doi.org/10.1021/acsomega.3c08285
ACS Omega 2024, 9, 19824−19836

5400, Bangladesh; orcid.org/0000-0002-0090-2384; Email: ferdousapee@gmail.com
Abdul Kuddus − *Ritsumeikan Global Innovation Research Organization, Ritsumeikan University, Shiga 525-8577, Japan;* orcid.org/0000-0001-5204-3844; Email: kuddus4910@gmail.com
Avijit Ghosh − *Advanced Energy Materials and Solar Cell Research Laboratory, Department of Electrical and Electronic Engineering, Begum Rokeya University, Rangpur 5400, Bangladesh;* orcid.org/0009-0000-8044-7686; Email: avijitghosheee@gmail.com

Authors

Md. Selim Reza − *Advanced Energy Materials and Solar Cell Research Laboratory, Department of Electrical and Electronic Engineering, Begum Rokeya University, Rangpur 5400, Bangladesh*
Mustafa K. A. Mohammed − *College of Engineering, University of Warith Al-Anbiyaa, Karbala 56001, Iraq;* orcid.org/0000-0002-1850-6355
Debashish Pal − *Department of Material Science and Engineering, Tripura University, Agartala 799022, India*
Md. Rasidul Islam − *Department of Electrical and Electronic Engineering, Bangamata Sheikh Fojilatunnesa Mujib Science & Technology University, Jamalpur 2012, Bangladesh;* orcid.org/0000-0002-9916-793X
Sagar Bhattarai − *Technology Innovation and Development Foundation, Indian Institute of Technology Guwahati, Guwahati 781039 Assam, India;* orcid.org/0000-0002-4805-9613
Ibrahim A. Shaaban − *Department of Chemistry, Faculty of Science, King Khalid University, Abha 61421, Saudi Arabia*
Mongi Amami − *Department of Chemistry, Faculty of Science, King Khalid University, Abha 61421, Saudi Arabia*

Complete contact information is available at: https://pubs.acs.org/10.1021/acsomega.3c08285

Author Contributions

M.F.R., A.K.: conceptualization, methodology, software, validation, formal analysis, visualization, investigation, data curation, supervision, writing-original draft, review and editing. M.S.R.: methodology, software, validation, formal analysis, visualization investigation, data curation, writing-original draft, review and editing, M.K.A.M., D.P., A.G., M.R.I.: validation, formal analysis, writing-original draft, review and editing. S.B., I.A.S., M.A.: methodology, formal analysis, writing-original draft, review and editing.

Notes

All authors declare that the manuscript does not contain studies on human subjects, human data or tissues, or animals. The authors declare no competing financial interest.

■ ACKNOWLEDGMENTS

The authors extend their appreciation to the Deanship of Scientific Research at King Khalid University for funding this work through large group Research Project under grant number R.G.P.2/521/44.

■ LIST OF ABBREVIATIONS

$RbPbBr_3$	rubidium−lead−bromide
N_D (N_A)	shallow identical donor (acceptor) density
EA, χ	electron affinity
ϵ_r	dielectric permittivity (relative)
$\mu_n(\mu_h)$	electron (hole) mobility
SCAPS	solar cell capacitance simulator
CB	conduction band
VB	valence band
EBD	energy band diagram
ETL(HTL)	electron (hole) transport layer
J_{sc}	short-circuit current density
FF	fill factor
PCE	power conversion efficiency
$J-V$	current density−voltage
N_C (N_V)	conduction (valence) band effective density of states
N_t	defect density
FTO	fluorine-doped tin oxide
PSC	perovskite solar cell
CBO	conduction band offset
VBO	valence band offset
SRH	Shockley−Read−Hall
WF	work function
PV	photovoltaic
R_s (R_{sh})	series (shunt) resistance
V_{oc}	open-voltage current
QE	quantum efficiency

■ REFERENCES

(1) Rahman, F.; Rahman, H.; Islam, R.; Hossain, M. K. Materials The Optical and Electronic Properties of Inorganic Halide Perovskite Sr 3 NCl 3 under Applied Biaxial Strain. *J. Mater. Sci.* **2023**.
(2) Shanto, A. B.; Rahman, F.; Islam, R.; Ghosh, A.; Azzouz-rached, A.; Albalawi, H.; Mahmood, Q. Investigating How the Electronic and Optical Properties of a Novel Cubic Inorganic Halide Perovskite, Sr 3 NI 3 Are Affected by Strain [Version 1 ; Peer Review : Awaiting Peer Review]. 2023.
(3) Ghosh, A.; Rahman, M. F.; Islam, M. R.; Islam, M. S.; Amami, M.; Hossain, M. K.; Md Ismail, A. B. Inorganic Novel Cubic Halide Perovskite Sr3AsI3: Strain-Activated Electronic and Optical Properties. *Heliyon* **2023**, *9* (8), No. e19271.
(4) Rahman, M. F.; Rahman, M. A.; Islam, M. R.; Ghosh, A.; Bashar Shanto, M. A.; Chowdhury, M.; Al Ijajul Islam, M.; Rahman, M. H.; Hossain, M. K.; Islam, M. A. Unraveling the Strain-Induced and Spin-Orbit Coupling Effect of Novel Inorganic Halide Perovskites of Ca3AsI3 Using DFT. *AIP Adv* **2023**, *138*, No. 085329.
(5) Rahman, F. Investigation of a Novel Inorganic Cubic Perovskite Ca 3 PI 3 with Unique Strain-Driven Optical, Electronic, and Mechanical Properties. *Nano Select* **2023**, *4*, 632−645.
(6) Ghosh, A.; Rahman, F.; Islam, R.; Islam, S.; Ghosh, A.; Rahman, F.; Islam, R. Structural, Electronic and Optical Characteristics of Inorganic Novel Cubic Perovskite Sr 3 AsI 3. *Opt. Continuum* **2023**, 2144−2153.
(7) Hossain, M. K.; Toki, G. F. I.; Alam, I.; Pandey, R.; Samajdar, D. P.; Rahman, M. F.; Islam, M. R.; Rubel, M. H. K.; Bencherif, H.; Madan, J.; Mohammed, M. K. A. Numerical Simulation and Optimization of CsPbI3-Based Perovskite Solar Cell to Enhance the Power Conversion Efficiency. *New J. Chem.* **2023**, *47*, 4801−4817.
(8) Hossain, M. K.; Arnab, A. A.; Das, R. C.; Hossain, K. M.; Rubel, M. H. K.; Rahman, M. F.; Bencherif, H.; Emetere, M. E.; Mohammed, M. K. A.; Pandey, R. Combined DFT, SCAPS-1D, and WxAMPS Frameworks for Design Optimization of Efficient Cs2BiAgI6-Based Perovskite Solar Cells with Different Charge Transport Layers. *RSC Adv.* **2022**, *12* (54), 34850−34873.
(9) Hossain, M. K.; Uddin, M. S.; Toki, G. F. I.; Mohammed, M. K. A.; Pandey, R.; Madan, J.; Rahman, F.; Islam, R.; Bhattarai, S.; Bencherif, H.; Samajdar, D. P.; Amami, M.; Dwivedi, D. K. RSC Advances Achieving above 24% e Ffi Ciency with Non-Toxic

Potential of the Absorber and Charge Transport. *RSC Adv.* **2023**, *13*, 23514−23537.
(10) Hossain, M. K.; Bhattarai, S.; Arnab, A. A.; Mohammed, M. K. A.; Pandey, R.; Ali, H.; Rahman, F.; Islam, R.; Samajdar, D. P.; Madan, J.; Bencherif, H.; Dwivedi, D. K.; Amami, M. RSC Advances Harnessing the Potential of CsPbBr 3 -Based Perovskite Solar Cells Using e Ffi Cient Charge Transport Materials and Global Optimization. *RSC Adv.* **2023**, *13*, 21044−21062.
(11) Qiao, T.; Parobek, D.; Dong, Y.; Ha, E.; Son, D. H. Photoinduced Mn Doping in Cesium Lead Halide Perovskite Nanocrystals. *Nanoscale* **2019**, *11* (12), 5247−5253.
(12) Zou, S.; Liu, Y.; Li, J.; Liu, C.; Feng, R.; Jiang, F.; Li, Y.; Song, J.; Zeng, H.; Hong, M.; Chen, X. Stabilizing Cesium Lead Halide Perovskite Lattice through Mn(II) Substitution for Air-Stable Light-Emitting Diodes. *J. Am. Chem. Soc.* **2017**, *139* (33), 11443−11450.
(13) Rubel, M. H. K.; Hossain, M. A.; Hossain, M. K.; Hossain, K. M.; Khatun, A. A.; Rahaman, M. M.; Ferdous Rahman, M.; Hossain, M. M.; Hossain, J. First-Principles Calculations to Investigate Structural, Elastic, Electronic, Thermodynamic, and Thermoelectric Properties of CaPd3B4O12 (B = Ti, V) Perovskites. *Results Phys.* **2022**, *42*, No. 105977.
(14) Hossain, M. K.; Toki, G. F. I.; Alam, I.; Pandey, R.; Samajdar, D. P.; Rahman, M. F.; Islam, M. R.; Rubel, M. H. K.; Bencherif, H.; Madan, J.; Mohammed, M. K. A. Numerical Simulation and Optimization of a CsPbI3-Based Perovskite Solar Cell to Enhance the Power Conversion Efficiency. *New J. Chem.* **2023**, *47* (10), 4801−4817.
(15) Rubel, M. H. K.; Mitro, S. K.; Hossain, M. K.; Hossain, K. M.; Rahaman, M. M.; Hossain, J.; Mondal, B. K.; Akter, A.; Rahman, M. F.; Ahmed, I.; Islam, A. K. M. A. First-Principles Calculations to Investigate Physical Properties of Single-Cubic (Ba0.82K0.18)-(Bi0.53Pb0.47)O3 Novel Perovskite Superconductor. *Mater. Today Commun.* **2022**, *33*, No. 104302.
(16) Hossain, M. K.; Samajdar, D. P.; Das, R. C.; Arnab, A. A.; Rahman, M. F.; Rubel, M. H. K.; Islam, M. R.; Bencherif, H.; Pandey, R.; Madan, J.; Mohammed, M. K. A. Design and Simulation of Cs2BiAgI6 Double Perovskite Solar Cells with Different Electron Transport Layers for Efficiency Enhancement. *Energy Fuels* **2023**, *37* (5), 3957−3979.
(17) Hossain, M. K.; Islam, R.; Rahman, F.; Bhattarai, S.; Bencherif, H.; Mohammed, M. K. A.; Pandey, R.; Madan, J.; et al. Photovoltaic Performance Investigation of Cs 3 Bi 2 I 9 - Based Perovskite 2 Solar Cells with Various Charge Transport Channels Using Density 3 Functional Theory and One-Dimensional Solar Cell Capacitance 4 Simulator Frameworks. *Energy Fuels* **2023**, *37*, 7380−7400.
(18) Bhattarai, S.; Hossain, M. K.; Pandey, R.; Madan, J.; Samajdar, D. P.; Rahman, M. F.; Ansari, M. Z.; Amami, M. Perovskite Solar Cells with Dual Light Absorber Layers for Performance Efficiency Exceeding 30%. *Energy Fuels* **2023**, *37*, 10631.
(19) Hossain, M. K.; Mohammed, M. K. A.; Pandey, R.; Arnab, A. A.; Rubel, M. H. K.; Hossain, K. M.; Ali, M. H.; Rahman, M. F.; Bencherif, H.; Madan, J.; Islam, M. R.; Samajdar, D. P.; Bhattarai, S. Numerical Analysis in DFT and SCAPS-1D on the Influence of Different Charge Transport Layers of CsPbBr3 Perovskite Solar Cells. *Energy Fuels* **2023**, *37* (8), 6078−6098.
(20) Hossain, M. K.; Sheikh, B.; Mujib, F.; Chandra, R.; Kumar, D.; et al. Design Insights of La2NiMnO6-Based Perovskite Solar Cell Employing Different Charge Transport Layers : DFT and SCAPS-1D Frameworks. *Energy Fuels* **2023**, 13377−13396.
(21) Hossain, M. K.; Toki, G. F. I.; Kuddus, A.; Rubel, M. H. K.; Hossain, M. M.; Bencherif, H.; Rahman, M. F.; Islam, M. R.; Mushtaq, M. An Extensive Study on Multiple ETL and HTL Layers to Design and Simulation of High-Performance Lead-Free CsSnCl3-Based Perovskite Solar Cells. *Sci. Rep.* **2023**, *13* (1), No. 2521.
(22) Zhou, W.; Zhao, Y.; Zhou, X.; Fu, R.; Li, Q.; Zhao, Y.; Liu, K.; Yu, D.; Zhao, Q. Light-Independent Ionic Transport in Inorganic Perovskite and Ultrastable Cs-Based Perovskite Solar Cells. *J. Phys. Chem. Lett.* **2017**, *8* (17), 4122−4128.
(23) Islam, R.; Liu, K.; Wang, Z.; Hasan, S.; Wu, Y.; Qu, S.; Wang, Z. Strain-Induced Electronic and Optical Properties of Inorganic Lead Halide Perovskites APbBr3 (A = Rb and Cs). *Mater. Today Commun.* **2022**, *31*, No. 103305.
(24) Wang, Y.; Zhang, T.; Kan, M.; Zhao, Y. Bifunctional Stabilization of All-Inorganic α-CsPbI 3 Perovskite for 17% Efficiency Photovoltaics. *J. Am. Chem. Soc.* **2018**, *140* (39), 12345−12348.
(25) Zhang, T.; Dar, M. I.; Li, G.; Xu, F.; Guo, N.; Grätzel, M.; Zhao, Y. Bication Lead Iodide 2D Perovskite Component to Stabilize Inorganic α-CsPbI 3 Perovskite Phase for High-Efficiency Solar Cells. *Sci. Adv.* **2017**, *3* (9), No. e1700841.
(26) Li, B.; Zhang, Y.; Fu, L.; Yu, T.; Zhou, S.; Zhang, L.; Yin, L. Surface Passivation Engineering Strategy to Fully-Inorganic Cubic CsPbI3 Perovskites for High-Performance Solar Cells. *Nat. Commun.* **2018**, *9* (1), No. 1076.
(27) Cha, M.; Da, P.; Wang, J.; Wang, W.; Chen, Z.; Xiu, F.; Zheng, G.; Wang, Z.-S. Enhancing Perovskite Solar Cell Performance by Interface Engineering Using CH 3 NH 3 PbBr 0.9 I 2.1 Quantum Dots. *J. Am. Chem. Soc.* **2016**, *138* (27), 8581−8587.
(28) Sanehira, E. M.; Marshall, A. R.; Christians, J. A.; Harvey, S. P.; Ciesielski, P. N.; Wheeler, L. M.; Schulz, P.; Lin, L. Y.; Beard, M. C.; Luther, J. M. Enhanced Mobility CsPbI 3 Quantum Dot Arrays for Record-Efficiency, High-Voltage Photovoltaic Cells. *Sci. Adv.* **2017**, *3* (10), No. eaao4204.
(29) Liang, J.; Liu, Z.; Qiu, L.; Hawash, Z.; Meng, L.; Wu, Z.; Jiang, Y.; Ono, L. K.; Qi, Y. Enhancing Optical, Electronic, Crystalline, and Morphological Properties of Cesium Lead Halide by Mn Substitution for High-Stability All-Inorganic Perovskite Solar Cells with Carbon Electrodes. *Adv. Energy Mater.* **2018**, *8* (20), No. 1800504.
(30) Rahman, M. F.; Alam Moon, M. M.; Hossain, M. K.; Ali, M. H.; Haque, M. D.; Kuddus, A.; Hossain, J.; Abu, A. B. Concurrent Investigation of Antimony Chalcogenide (Sb2Se3 and Sb2S3)-Based Solar Cells with a Potential WS2 Electron Transport Layer. *Heliyon* **2022**, *8* (12), No. e12034.
(31) Rahman, M. F.; Habib, M. J. A.; Ali, M. H.; Rubel, M. H. K.; Islam, M. R.; Md Ismail, A. B.; Hossain, M. K. Design and Numerical Investigation of Cadmium Telluride (CdTe) and Iron Silicide (FeSi 2) Based Double Absorber Solar Cells to Enhance Power Conversion Efficiency. *AIP Adv.* **2022**, *12* (10), No. 105317.
(32) Ke, W.; Fang, G.; Wan, J.; Tao, H.; Liu, Q.; Xiong, L.; Qin, P.; Wang, J.; Lei, H.; Yang, G.; Qin, M.; Zhao, X.; Yan, Y. Efficient Hole-Blocking Layer-Free Planar Halide Perovskite Thin-Film Solar Cells. *Nat. Commun.* **2015**, *6* (1), No. 6700.
(33) Liu, D.; Yang, J.; Kelly, T. L. Compact Layer Free Perovskite Solar Cells with 13.5% Efficiency. *J. Am. Chem. Soc.* **2014**, *136* (49), 17116−17122.
(34) Ghebouli, M. A.; Ghebouli, B.; Larbi, R.; Chihi, T.; Fatmi, M. Effect of Buffer Nature, Absorber Layer Thickness and Temperature on the Performance of CISSe Based Solar Cells, Using SCAPS-1D Simulation Program. *Optik* **2021**, *241*, No. 166203.
(35) Chu, W.; Li, X.; Li, S.; Hou, J.; Jiang, Q.; Yang, J. High-Performance Flexible Perovskite Solar Cells with a Metal Sulfide Electron Transport Layer of SnS2 by Room-Temperature Vacuum Deposition. *ACS Appl. Energy Mater.* **2019**, *2* (1), 382−388.
(36) Subudhi, P.; Punetha, D. Pivotal Avenue for Hybrid Electron Transport Layer-Based Perovskite Solar Cells with Improved Efficiency. *Sci. Rep.* **2023**, *13* (1), No. 19485.
(37) Rahman, M. F.; Islam, R.; Ghosh, A.; et al. Exploring the Impact of Strain on the Electronic and Optical Properties of Inorganic Novel Cubic Perovskite Sr 3 PI 3. *Phys. Scr.* **2023**, *98* (11), No. 115105.
(38) Kuddus, A.; Mohammed, M. K. A.; Al-mousoi, A. K.; Ghosh, A.; Bhattarai, S.; Pandey, R.; Madan, J.; Hossain, M. K. Boosting efficiency above 28% using effective charge transport layer with Sr3SbI3 based novel inorganic perovskite. *RSC Adv.* **2023**, 31330−31345.
(39) Islam, M. S.; Rahman, M. F.; Islam, M. R.; Ghosh, A.; Monnaf, M. A.; Reza, M. S.; Hossain, M. K.; Zaman, A.; Ezzine, S.; Ben Farhat, L. An In-Depth Analysis of How Strain Impacts the Electronic,

https://doi.org/10.1021/acsomega.3c08285
ACS Omega 2024, 9, 19824−19836

Optical, and Output Performance of the Ca3NI3 Novel Inorganic Halide Perovskite. *J. Phys. Chem. Solids* **2024**, *185*, No. 111791.
(40) Burgelman, M.; Nollet, P.; Degrave, S. Modelling Polycrystalline Semiconductor Solar Cells. *Thin Solid Films* **2000**, *361−362*, 527−532.
(41) Ali, M. H.; Al Mamun, M. A.; Haque, M. D.; Rahman, M. F.; Hossain, M. K.; Md Touhidul Islam, A. Z. Performance Enhancement of an MoS 2 -Based Heterojunction Solar Cell with an In 2 Te 3 Back Surface Field: A Numerical Simulation Approach. *ACS Omega* **2023**, *8* (7), 7017−7029.
(42) Rahman, M. F.; Harun-Or-Rashid, M.; Islam, M. R.; Ghosh, A.; Hossain, M. K.; Bhattarai, S.; Pandey, R.; Madan, J.; Ali, M. A.; Ismail, A. B. M. Exploring the Impact of Strain on the Electronic and Optical Properties of Inorganic Novel Cubic Perovskite Sr3PI3. *Phys. Scr.* **2023**, *98*, No. 115105.
(43) Rahman, M. F.; Islam, M. M.; Islam, M. R.; Ghosh, A.; Rahman, M. A.; Rahman, M. H.; Islam, M. A. I.; Islam, M. A.; Albalawi, H.; Mahmood, Q. An Investigation on Strain-Incited Electronic and Optical Properties of Novel Inorganic Cubic Material Sr3AsCl3. *J. Solid State Chem.* **2023**, *328*, No. 124341.
(44) Rahman, F.; et al. First-Principles Analysis of How Cobalt Doping Affects the Structural, Electronic, and Optical Properties of a-MoO3. *Indian J. Phys.* **2023**, 1−10.
(45) Rahman, M. F.; Habib, M. J. A.; Ali, M. H.; Rubel, M. H. K.; Islam, M. R.; Abu, A. B.; Hossain, M. K. Design and Numerical Investigation of Cadmium Telluride (CdTe) and Iron Silicide (FeSi2) Based Double Absorber Solar Cells to Enhance Power Conversion Efficiency. *AIP Adv.* **2022**, *12* (10), No. 105317.
(46) Roy, S.; Bermel, P. Electronic and Optical Properties of Ultra-Thin 2D Tungsten Disulfide for Photovoltaic Applications. *Sol. Energy Mater. Sol. Cells* **2018**, *174*, 370−379.
(47) Alam, I.; Ashraf, M. A. Effect of Different Device Parameters on Tin-Based Perovskite Solar Cell Coupled with In 2 S 3 Electron Transport Layer and CuSCN and Spiro-OMeTAD Alternative Hole Transport Layers for High-Efficiency Performance. *Energy Sources, Part A* **2020**, 1−17.
(48) Kuddus, A.; et al. Role of Facile Synthesized V2O5 as Hole Transport Layer for CdS/CdTe Heterojunction Solar Cell: Validation of Simulation Using Experimental Data. *Superlattices Microstruct.* **2019**, No. 106168.
(49) Khoshsirat, N.; Md Yunus, N. A. Numerical Analysis of In2S3 Layer Thickness, Band Gap and Doping Density for Effective Performance of a CIGS Solar Cell Using SCAPS. *J. Electron. Mater.* **2016**, *45* (11), 5721−5727.
(50) Alam, I.; Mollick, R.; Ashraf, M. A. Numerical Simulation of Cs2AgBiBr6-Based Perovskite Solar Cell with ZnO Nanorod and P3HT as the Charge Transport Layers. *Phys. B* **2021**, *618*, No. 413187.
(51) Mandadapu, U. Simulation and Analysis of Lead Based Perovskite Solar Cell Using SCAPS-1D. *Indian J. Sci. Technol.* **2017**, *10* (1), 1−8.
(52) Lin, L.; Jiang, L.; Li, P.; Fan, B.; Qiu, Y. A Modeled Perovskite Solar Cell Structure with a Cu2O Hole-Transporting Layer Enabling over 20% Efficiency by Low-Cost Low-Temperature Processing. *J. Phys. Chem. Solids* **2019**, *124*, 205−211.
(53) Bag, A.; Radhakrishnan, R.; Nekovei, R.; Jeyakumar, R. Effect of Absorber Layer, Hole Transport Layer Thicknesses, and Its Doping Density on the Performance of Perovskite Solar Cells by Device Simulation. *Sol. Energy* **2020**, *196*, 177−182.
(54) Liu, D.; Gangishetty, M. K.; Kelly, T. L. Effect of CH 3 NH 3 PbI 3 Thickness on Device Efficiency in Planar Heterojunction Perovskite Solar Cells. *J. Mater. Chem. A* **2014**, *2* (46), 19873−19881.
(55) Tareq, D. E.; AbdulAlmohsin, S. M.; Waried, H. H. Efficiency of TiO 2 /Peroviskites/Cu 2 O Solar Cells with Optimal Thickness at Varying of Environment Temperature. *IOP Conf. Ser.: Mater. Sci. Eng.* **2020**, *928* (7), No. 072044.
(56) Patel, P. K. Device Simulation of Highly Efficient Eco-Friendly CH3NH3SnI3 Perovskite Solar Cell. *Sci. Rep.* **2021**, *11* (1), No. 3082.
(57) Jayan, K. D.; Sebastian, V. Comparative Performance Analysis of Mixed Halide Perovskite Solar Cells with Different Transport Layers and Back Metal Contacts. *Semicond. Sci. Technol.* **2021**, *36* (6), No. 065010.
(58) Tara, A.; Bharti, V.; Sharma, S.; Gupta, R. Device Simulation of FASnI3 Based Perovskite Solar Cell with Zn(O0.3, S0.7) as Electron Transport Layer Using SCAPS-1D. *Opt. Mater.* **2021**, *119*, No. 111362.
(59) Samiul Islam, M.; Sobayel, K.; Al-Kahtani, A.; Islam, M. A.; Muhammad, G.; Amin, N.; Shahiduzzaman, M.; Akhtaruzzaman, M. Defect Study and Modelling of SnX3-Based Perovskite Solar Cells with SCAPS-1D. *Nanomaterials* **2021**, *11* (5), 1218.
(60) Gupta, G. K.; Garg, A.; Dixit, A. Electrical and Impedance Spectroscopy Analysis of Sol-Gel Derived Spin Coated Cu2ZnSnS4 Solar Cell. *J. Appl. Phys.* **2018**, *123* (1), No. 013101.
(61) Ferdiansjah; Faridah; Mularso, K. T. Analysis of Back Surface Field (BSF) Performance in P-Type And N-Type Monocrystalline Silicon Wafer. *E3S Web Conf.* **2018**, *43*, No. 01006.
(62) Ahmad, O.; Rashid, A.; Ahmed, M. W.; Nasir, M. F.; Qasim, I. Performance Evaluation of Au/p-CdTe/Cs2TiI6/n-TiO2/ITO Solar Cell Using SCAPS-1D. *Opt. Mater.* **2021**, *117*, No. 111105.
(63) Zhou, Y.; Gray-Weale, A. A Numerical Model for Charge Transport and Energy Conversion of Perovskite Solar Cells. *Phys. Chem. Chem. Phys.* **2016**, *18* (6), 4476−4486.
(64) Behrouznejad, F.; Shahbazi, S.; Taghavinia, N.; Wu, H.-P.; Wei-Guang Diau, E. A Study on Utilizing Different Metals as the Back Contact of CH 3 NH 3 PbI 3 Perovskite Solar Cells. *J. Mater. Chem. A* **2016**, *4* (35), 13488−13498.
(65) Raga, S. R.; Barea, E. M.; Fabregat-Santiago, F. Analysis of the Origin of Open Circuit Voltage in Dye Solar Cells. *J. Phys. Chem. Lett.* **2012**, *3* (12), 1629−1634.
(66) Eperon, G. E.; Paternò, G. M.; Sutton, R. J.; Zampetti, A.; Haghighirad, A. A.; Cacialli, F.; Snaith, H. J. Inorganic Caesium Lead Iodide Perovskite Solar Cells. *J. Mater. Chem. A* **2015**, *3* (39), 19688−19695.
(67) Hossain, J.; Moon, M. M. A.; Mondal, B. K.; Halim, M. A. Design Guidelines for a Highly Efficient High-Purity Germanium (HPGe)-Based Double-Heterojunction Solar Cell. *Opt. Laser Technol.* **2021**, *143*, No. 107306.
(68) Moon, M. M. A.; Ali, M. H.; Rahman, M. F.; Kuddus, A.; Hossain, J.; Ismail, A. B. M. Investigation of Thin-Film p -BaSi 2/n -CdS Heterostructure towards Semiconducting Silicide Based High Efficiency Solar Cell. *Phys. Scr.* **2020**, *95* (3), No. 035506.
(69) Reza, M. S.; Rahman, M. F.; Kuddus, A.; Mohammed, M. K. A.; Al-Mousoi, A. K.; Islam, M. R.; Ghosh, A.; Bhattarai, S.; Pandey, R.; Madan, J.; Hossain, M. K. Boosting Efficiency above 28% Using Effective Charge Transport Layer with Sr 3 SbI 3 Based Novel Inorganic Perovskite. *RSC Adv.* **2023**, *13* (45), 31330−31345.

https://doi.org/10.1021/acsomega.3c08285
ACS Omega 2024, 9, 19824−19836